Geochemistry, Geophysics, Geosystems®

Key Points:

- Azimuthal variations in receiver functions reveal oriented tectonic fabrics across the arc-continent collision zone in Banda
- Orogen- and convergence-parallel oriented fabrics imaged on Timor and Alor are interpreted as orogenic and strike-slip structures
- Oriented fabrics imaged on inner arc islands of Flores and Lomblen are likely associated with variable volcanic structures

Supporting Information:

Supporting Information may be found in the online version of this article.

Correspondence to:

P. Zhang,
ping.zhang@anu.edu.au

Tectonic Fabric in the Banda Arc-Australian Continent Collisional Zone Imaged by Teleseismic Receiver Functions

Ping Zhang[1,2], **Meghan S. Miller[1]**, and **Vera Schulte-Pelkum[3,4]**

[1]Research School of Earth Sciences, Australian National University, Canberra, ACT, Australia, [2]Deep Earth Imaging, Future Science Platform, CSIRO, Perth, WA, Australia, [3]Cooperative Institute for Research in Environmental Sciences, University of Colorado Boulder, Boulder, CO, USA, [4]Department of Geological Sciences, University of Colorado Boulder, Boulder, CO, USA

Abstract The convergent plate boundary in eastern Indonesia and Timor-Leste captures an active oblique collision between the Banda Arc and the Australian plate. We analyzed ~5 years' worth (2014–2019) of radial and tangential teleseismic Ps receiver functions (RFs) observed at 30 temporary broadband seismic stations across the area. Azimuthal variations in RF arrivals are observed throughout the region, indicative of the presence of oriented tectonic fabrics (dipping contrasts or plunging axis anisotropy) from a variety of crustal depths. The two main strikes of these fabrics are roughly parallel to the orogen and the plate convergence across the outer arc islands, likely associated with orogenic and strike-slip structures. We observe distinct double polarity-reversal arrivals with opposite polarity that reflect an anisotropic layer with orogen-parallel strikes in the shallow crust beneath Timor and Savu, interpreted as metamorphic rocks. Fabrics oriented E-W are imaged beneath the Flores and Lomblen that host active volcanoes, where we find interesting correlations with magmatic structures. NNW-SSE striking fabric is imaged at ~13 km depth beneath central Flores, which relates to a connected dike magmatic system that feeds the aligned cinder cones exposed on the surface. Finally, we identify convergence-parallel fabrics on the volcano-extinct islands of Alor and Atauro, consistent with one main fabric orientation imaged in Timor. We suggest all convergence-parallel fabrics might accommodate strike-slip motion generated by the overall NNE convergence of the Australian plate with respect to Eurasian plate and contribute to strain partitioning between the trough and backarc resulting from the collision.

Plain Language Summary We used ~5 years of seismic data collected at 30 temporary seismic stations to aid in understanding the evolution of the Banda Arc-Australian plate collision. The seismometers were deployed between 2014 and 2019 across the islands of Eastern Indonesia and Timor-Leste in order to seismically image the structure of the deep Earth and infer more about the processes of plate collision. Here, we used a technique named receiver function analysis that images boundaries and changes in fabric of the rocks in the Earth's crust. The layers and structures we image at depth across the region reflect the complex tectonic history and variation in rock types that can be interpreted with complementary geological data. We find that the majority of the orientations of the deep crustal structures are roughly parallel to the orientation of the islands and new mountain formation. However, some of the imaged structures and fabrics are clearly related to active volcanoes and others are associated with the complex deformation of the crust during the recent collision of the Australian plate with the active volcanic arc.

1. Introduction

The Banda Arc-Australian continent collision in eastern Indonesia and Timor-Leste is exemplary of an incipient oblique arc-continent collision. From west to east, the incoming Indo-Australian plate structure transitions from Cretaceous to Jurassic age oceanic lithosphere (Müller et al., 2008) to continental margin lithosphere that is inherently heterogeneous (Harris, 2011; Keep & Haig, 2010; Spakman & Hall, 2010). To the north of the plate boundary, the transition in the incoming plate structure is evident in the linear single volcanic Sunda Arc bifurcating into a double chain of islands (Figure 1a). The northern chain of islands is referred to as the inner arc, composed of volcanic rocks of Neogene age. The southern chain of islands is the non-volcanic outer arc, formed by orogenic structures. The outer arc includes the NNE-SSW oriented islands of Timor, Savu, and Rote and the NNW-SSW striking Sumba Island between the Java Trench-Timor Trough system and the volcanic arc (Figure 1).
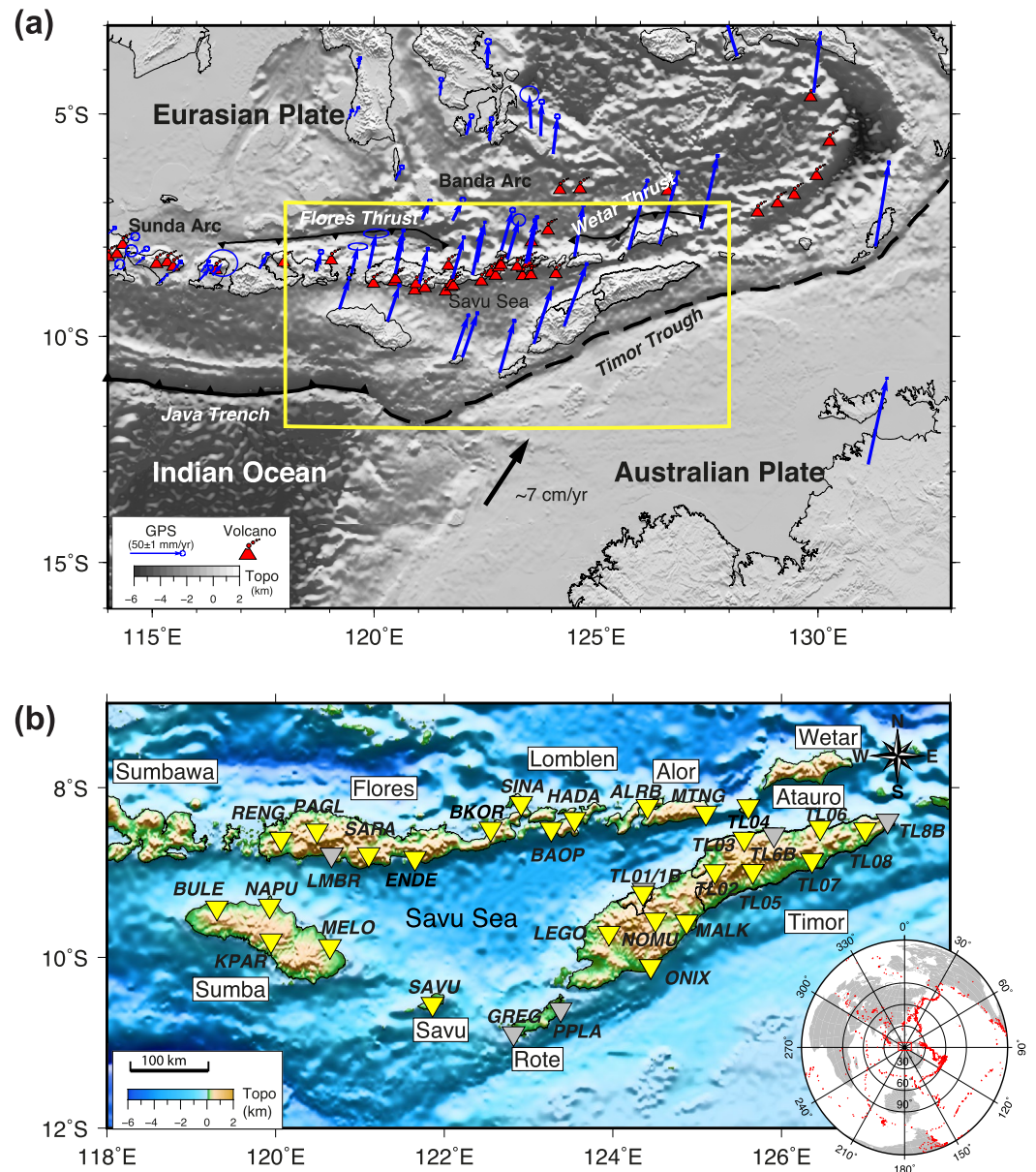
Figure 1. Tectonic setting and the Banda Arc seismic experiment. (a) Map of topography, GPS velocity field, and tectonics. Red triangles with bubbles represent active volcanoes from the Global Volcanism Program, Smithsonian Institution (2013). Black solid line with sided triangles in north and black dashed line mark the Java Trench and Timor Trough, respectively (modified after Hall, 2017; Pownall et al., 2013). Flores and Wetar thrusts are modified from Silver et al. (1983) and Koulali et al. (2016). Blue vectors with ellipses are GPS velocities and their 95% confidence level measured by Koulali et al. (2016). The black arrow represents relative plate motion from the NUVEL-1A model (DeMets et al., 1994). Black solid line outlines the country boundary of Timor-Leste including the Oecusse enclave in West Timor and Atauro Island. The yellow rectangle in the center outlines the location of the map in panel (b). Major plates referred to in the text are labeled. (b) 30 broadband seismic stations in the YS network, shown by the inverted triangles. Yellow triangles indicate stations used in azimuthal receiver function (RF) analyses. Gray triangles had results with large uncertainties or insufficient RF numbers for azimuthal analyses. Major islands referred to in the text are labeled inside white boxes. Inset global map is the distribution of teleseismic events (red dots) used in the analyses.

In the Banda Arc, coeval with the complex deformation of this tectonic transition, orogenesis and volcanism have been active on the outer and inner arc islands, which makes it difficult to unravel their evolution from data collected at the surface alone. The islands of Timor and Savu in the outer arc juxtapose rocks from both sides of the convergent plate boundary (Harris, 2011; Harris et al., 2009). The mountain belt of Timor consists

of imbricated and duplex sequences derived from the northwest shelf of Australia, locally overlain by fragments of the pre-collisional forearc complex or thrust nappes (e.g., Harris, 2011). Here, collision-related metamorphic rocks form a massif with mountainous topography (~3,000 m), extending along the whole length of the island (e.g., Harris, 2011; Kaneko et al., 2007). However, these orogenic islands began emerging from the sea only ~3 Ma ago (Haig & McCartain, 2007). This young age means that the rocks exposed on the surface likely represent only the uppermost structural levels of a fold-and-thrust belt that is still largely not exposed (Keep & Haig, 2010). The inner arc islands have hosted volcanic activity since 4 Ma (Harris, 2011). There are distinct variations in volcanism and magmatic arc chemistry along the arc (e.g., Elburg et al., 2004, 2005; Hilton et al., 1992). Since 3 Ma, cessation of volcanism has spread from Wetar to the neighboring islands north of eastern Timor (Figure 1a; Honthaas et al., 1998). North of the volcanic front, there are two major back-arc thrusts identified in the study region: the Flores Thrust north of Sumbawa and western Flores and the Wetar thrust north of Timor (Figure 1; e.g., Silver et al., 1983). In the Banda Arc, it is thought that the plate convergence is partitioned between the Timor Trough deformation front and the back-arc system that is seismically active (Koulali et al., 2016; McCaffrey, 1988; Nugroho et al., 2009). However, there is little conclusive seismic evidence identifying the distribution of faults and other structures in the crust that might accommodate the deformation across the entire collisional zone. Within the confines of surface data, the complex geology and active tectonics have fed a high level of disagreement regarding the evolution of this plate boundary. For example, the proposed age for the collision varies from 18 Ma (Lytwyn et al., 2001; Rutherford et al., 2001), to post 9.8 Ma but before 5.7 Ma (Keep & Haig, 2010), to less than 4–2 Ma (Audley-Charles, 2004; Spakman & Hall, 2010). Deep structure inferred from seismic imaging studies, therefore, will be vital to address contested tectonic interpretations in Banda Arc.

In the study region, much of the existing knowledge of the crustal structure comes from localized offshore active-source studies (e.g., Fainstein et al., 2020; Petkovic et al., 2000; Shulgin et al., 2009). Onshore seismic instrumentation is relatively sparse and spatially constrained to the larger islands of the Indonesian Nusa Tenggara Timur (NTT) province. There are two operating permanent seismic stations (from the GE network) with open-access data and seven temporary stations (from the IA network) supported by the Indonesian government sporadically distributed across West Timor, Sumba, and Flores islands. Some of smaller islands (Lomblen, Alor, and Savu) as well as Timor-Leste that includes East Timor, the Oecusse enclave in West Timor, and Atauro Island in this region (Figure 1b) have been mostly unexplored seismologically prior to the experiment in this study. A previous study (Syuhada et al., 2016) used the existing stations from the GE and IA networks to derive one-dimensional (1-D) crustal shear-wave velocity (Vs) profiles based on classic radial receiver function (RF) analysis of waveform inversion and H-k stacking. These analyses assumed that the Earth's model is isotropic and flat-layered. The complicated and azimuthally varying RF waveforms shown in their paper, however, indicate the breakdown of this assumption. Similar RF signals have been used elsewhere to infer lithospheric anisotropy and its tectonic implications (e.g., Audet, 2015; Bar et al., 2019; Birkey et al., 2021; Bourke et al., 2020; Chen et al., 2021; Frothingham et al., 2022; Gosselin et al., 2021; Levin et al., 2021; Nikulin et al., 2019; Olugboji et al., 2016; Salimbeni et al., 2021; Schulte-Pelkum et al., 2021; Sherrington et al., 2004; Vergne et al., 2003). In addition, the small number of RF measurements (<20–60 for more than half of stations) considered in Syuhada et al. (2016) may lead to uncertainties in their results. Therefore, imaging with improved data coverage and with methods that consider non-isotropic energy in RFs will provide substantially more information about the crustal structure across the wider region.

Recently, a new Banda Arc seismic experiment (Figure 1b; Miller et al., 2016) offers a dense data set to examine the detailed lithospheric configuration at depth by passive seismology, which drastically improves our understanding of the geodynamic processes that govern the region. This array (coded as the YS network) includes the first broadband seismometer deployment in Timor-Leste and on the islands of Lomblen, Savu, Rote, and Alor in eastern Indonesia (Figure 1b; Miller et al., 2016). Using this data set, new imaging of crustal and mantle structure suggests continent subduction/underthrust is the dominant lithospheric structure beneath the region (Miller et al., 2021; Porritt et al., 2018; Zhang & Miller, 2021), in line with conclusions of other regional seismic tomography studies (e.g., Fichtner et al., 2010; Harris et al., 2020; Zenonos et al., 2019, 2020). The pronounced along-strike structural variations at shallow lithospheric depths may either result from the diachronous (progressive) collision as a result of the oblique convergence (Porritt et al., 2018; Zhang & Miller, 2021) or from inherent structural heterogeneities of the incoming and colliding Australian (lower) plate (Miller et al., 2021), or both. The present-day seismic structure may be further complicated by exotic terranes or microplates formed during the Jurassic breakup of eastern Gondwana (e.g., Supendi et al., 2020; Zhang & Miller, 2021). Most recently, Jiang

et al. (2022) offers a most complete catalog with data of the YS network, which describes a complex pattern of crustal events across the collisional zone and into the backarc, as well as abundant deep slab seismicity. Anisotropy is also investigated by Harris and Miller (in press) using shear wave splitting, which suggests potential along-strike variations in mantle dynamics. These recent findings imply that the deep structure across the region is extremely complex with dramatic along-strike and across-arc variations. Given the unusual subduction and collision tectonics, it is natural to expect that both anisotropic fabric and dipping layers together with strong isotropic seismic velocity jumps are ubiquitous in the study region. Mapping these seismic structures in the crust has proven to be particularly useful to understand tectonically active areas, such as in orogenic belts and volcanic arcs formed through collision and subduction (e.g., Bianchi et al., 2015; Schulte-Pelkum, Caine, et al., 2020; Schulte-Pelkum, Ross, et al., 2020; Schulte-Pelkum et al., 2005). Therefore, these structures are important to investigate in the study region where both orogenesis and volcanism are actively involved.

The purpose of this study is to image discontinuity and anisotropy structures in the crust using a new data set collected by the Banda Arc seismic experiment and discuss the different mechanisms and progresses that may have contributed to the evolution of the orogenic wedge, arc volcanism, and arc-continent collision. In the following, we first analyze the azimuthal variations from both radial and tangential RFs following Schulte-Pelkum and Mahan (2014a, 2014b). We provide a detailed description of how we identified and interpreted those prominent oriented fabrics from a variety of crustal depths. Last, we focus on the regional pattern of the fabric orientations and a few representative RF waveforms and discuss their tectonic implications with complementary surface data.

2. Data and Methods

The temporary deployment of the YS network includes 30 broadband stations across the eastern NTT region of Indonesia (22 stations) and Timor-Leste (8 stations) from March 2014 to August 2019 (Figure 1b; Miller, 2014; Miller et al., 2016). We analyzed three-component seismograms for P or P_{diff} phases from a total of 2,150 events with magnitude >5.5 and epicentral distance between 25° and 150° from the USGS NEIC global catalog recorded by the array (Figure 1b). Event coverage is dominated by the western and northern Pacific, Fiji-Tonga, and Central and South American corridors, with a backazimuth coverage from 0° to 50° (∼27%) and from 70° to 180° (>50%), and less regularly sampled otherwise (inset global map in Figure 1b). In general, these earthquakes reflect good coverage globally, which facilitates analyses of azimuthal variations in RF conversions that can image structural contrasts and anisotropic fabrics.

For each event, we extracted 120 s long data windows based on the theoretical P wave arrival times from the IASP91 velocity model (Kennett & Engdahl, 1991). Three-component seismograms were rotated into an R-T-Z coordinate system and band-pass filtered to frequencies of 0.03–4 Hz. These seismograms were then processed by removing the linear trend and the mean as well as applying a cosine taper with a width of 0.1 s. Next, we computed 27,838 RFs with both radial and tangential components by the time-domain iterative deconvolution algorithm (Ligorría & Ammon, 1999) with a Gaussian width of 3.0 using codes from Herrmann (2013). We screened the RFs by automated quality control following steps outlined in Schulte-Pelkum and Mahan (2014a): (a) the signal-to-noise ratio (noise window is 35 s before to 5 s after theoretical P onset and signal window is 5 s before and 25 s after theoretical P onset) of the initial vertical component is >1.0; (b) the fit to horizontal components of the convolution of the RF with vertical components is >60%; (c) the radial component RF shows a positive polarity direct P arrival that is the largest arrival in the trace; (d) the RF amplitude does not exceed 2; (e) any arrivals' pulse length does not exceed 3.5 s; and (f) any tangential component RF has a radial RF from the same event that passed quality control. In general, about 10% RFs pass the above quality control at each station. We discarded stations with azimuthal gaps larger than 90° in the azimuthal harmonic analysis. Finally, we retained radial and tangential RFs at 26 stations (yellow inverted triangles in Figure 1b) and stacked them into 10° backazimuth bins for further azimuthal analysis.

Dipping contrasts between isotropic layers or contrasts in P-wave anisotropy with a plunging symmetry axis on at least one side of an interface can generate observable RF arrivals that change polarity with backazimuth on both radial and tangential components (e.g., Levin & Park, 1998; Schulte-Pelkum & Mahan, 2014a, 2014b; Schulte-Pelkum, Caine, et al., 2020; Schulte-Pelkum, Ross, et al., 2020). To isolate these signals, we applied the procedures outlined by Schulte-Pelkum and Mahan (2014a, 2014b). The results are demonstrated by a representative station, NOMU, in Figure 2. These were produced by processing the moveout corrected radial and tangential
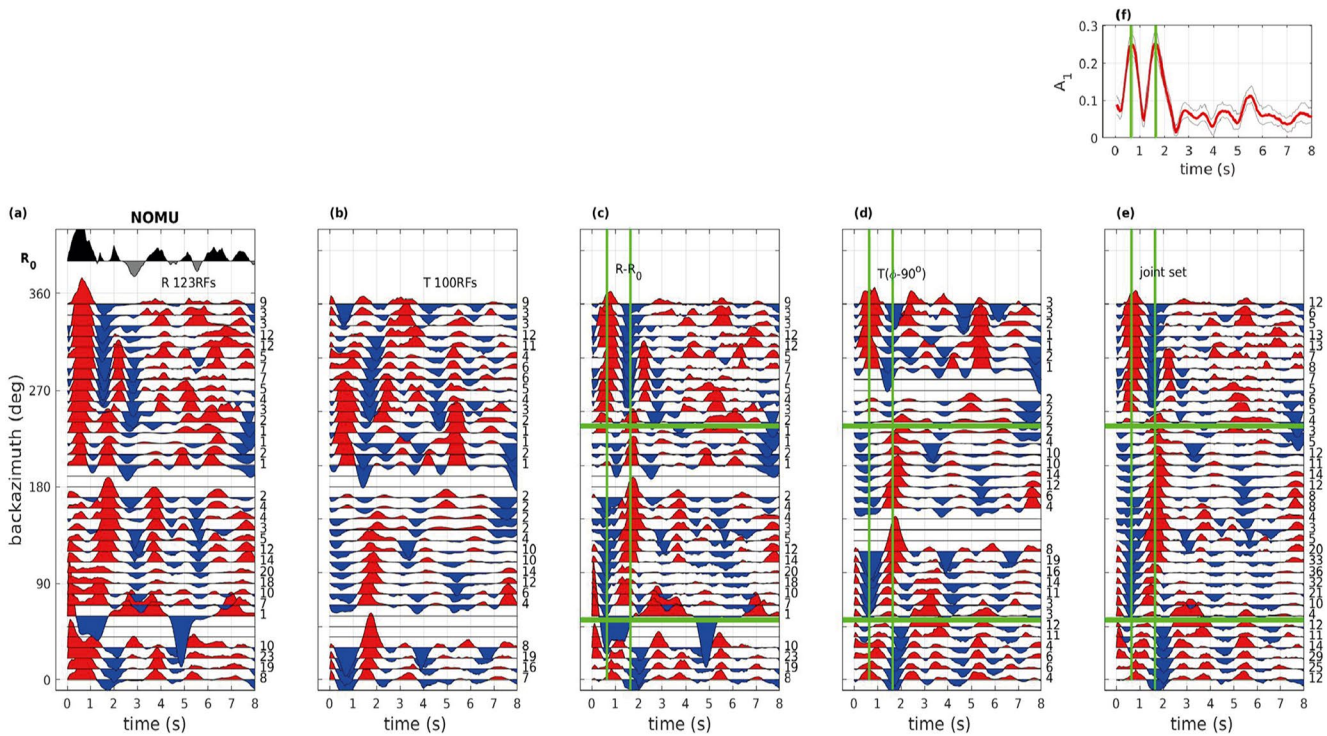
Figure 2. Azimuthal harmonic receiver function (RF) analysis for an example station NOMU in west Timor (see Figure 1b for its location). (a) Moveout-corrected radial RFs binned every 10° in backazimuth. Red and blue phases indicate positive and negative conversions. Trace at the top of the panel is the azimuthal average R_0, where black and gray are positive and negative amplitudes respectively. (b) Tangential RFs binned by back azimuth, else as in panel (a). (c) Processed radial component after R_0 (as shown in panel (a)) was subtracted from each bin trace. (d) Processed tangential component after shifting bin traces by 90° in backazimuth. (e) Composite set from panels ((c) [$R–R_0$] and (d) [shifted tangential component]) for harmonic analysis with moving window (2.5 s) to determine amplitude and phase of first azimuthal harmonic, A1, as shown in panel (f). For all subplots, numbers of RFs per bin are indicated on the right of each trace. Azimuthal smoothing was applied with a binning overlap of 5°. (f) A1 amplitude (red line) and 95% confidence interval (gray lines) at each time window. The maximum amplitude (A1$_{max}$) with its corresponding delay time is marked with green solid lines.

component RFs (Figures 2a and 2b) by: (a) subtracting the station average over backazimuth (R_0 in Figure 2a) from the radial component RFs (Figures 2a and 2c); (b) shifting the tangential component RFs by 90° clockwise in backazimuth (Figures 2b and 2d); and (c) combining the two and solving for degree-1 azimuthal harmonic (referred to as A1 or 360° periodic signal hereafter) in the joint set in a sliding time window of 0.25 s length (Figures 2e and 2f). The solution is represented by the A1 signal amplitude (Figure 2f) and phase at each time step. Identification of those peaks in the amplitude of the A1 signal (green lines in Figure 2f) effectively outlines strong conversions from either dipping interfaces or anisotropic structures beneath a station (e.g., A1 peaks outlined by vertical green lines in Figures 2c and 2d). RF waveforms for station NOMU shown in Figure 2 and for the other 25 stations shown in Figure 3 and in the supplement (Figures S1–S5 in Supporting Information S1) demonstrate that A1 signals are successfully detected.

For each picked A1 arrival, the best-resolved quantities are the strike and depth of the oriented structures that generate the conversions. The strike is constrained by the polarity flip nodes for the considered arrivals (horizontal green lines in Figures 2c and 2d), which are calculated by the phase of an A1 amplitude peak plus 90°. The depth is determined from the delay time of those considered arrivals (vertical green lines in Figure 2) and station-specific 1-D models. Each 1-D model was derived from a three-dimensional (3-D) crustal Vs model based on ambient noise tomography using the YS network data from Zhang and Miller (2021).

For each station, we also run bootstrapping that solves for amplitude and phase of the A1 signals by omitting random azimuthal bins in 100 instances and calculating a 95% confidence interval based on the resultant distribution. Gray lines in Figure 2f present an example of amplitude uncertainties. In the following analysis, we discarded those results with the amplitude uncertainty larger than 60% of the A1 amplitude. RF strike uncertainties are shown in Figure 4 and discussed in the next section.
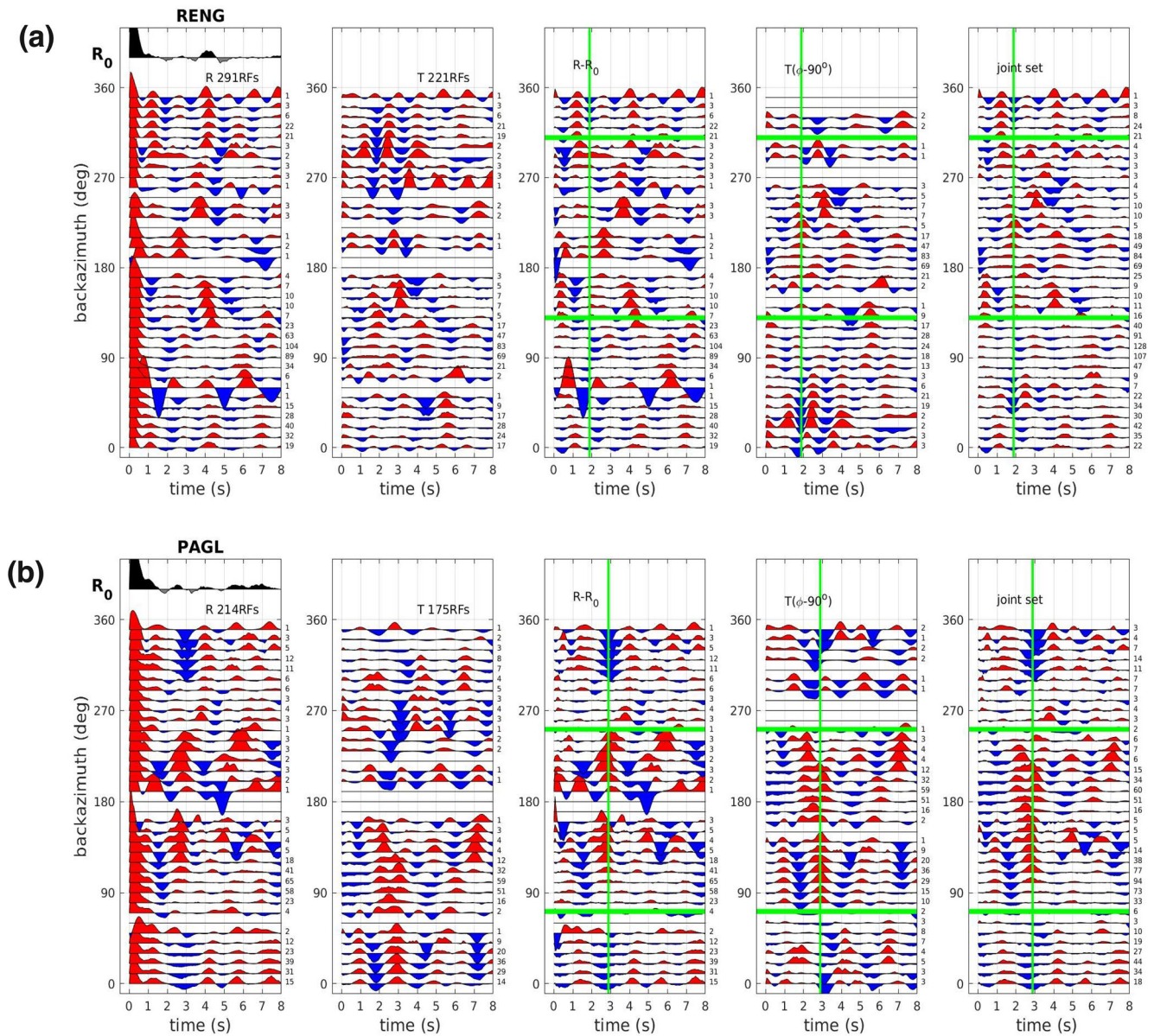
Figure 3. Receiver function (RF) waveforms and their harmonic analysis for station RENG (a) and PAGL (b) on the western Flores, SARA (c) on the central Flores, and ALRB (d) on Alor island (see Figure 1b for its location). Five panels in each plot are moveout-corrected radial and transverse RFs, processed radial and transverse RFs as well as the joint set of the processed components for harmonic analysis, respectively. Symbols and labels are the same as in Figure 2.

3. Results

In this study, we consider RFs in the first 8 s after the direct P arrival to focus on major direct conversions from the lithospheric structure. Results are presented in two forms: (a) map views of resolved parameters from the A1 arrivals in Figure 4 and (b) backazimuthal variations in the RF waveforms at each station in Figures 2 and 3 and Figures S1–S5 in Supporting Information S1.

In Figure 4a, we show a map of resolved A1 arrivals using its depth-averaged amplitude as a percentage of total RF amplitude within the first 8 s. The value provides a measure of how much of the total RF signal may be explained by contrasts with dipping foliation or other dipping structures in the considered time/depth range (Schulte-Pelkum, Caine, et al., 2020; Schulte-Pelkum, Ross, et al., 2020). We find that for most stations, over 30% of the amplitude in the RFs is found in the first azimuthal harmonic (Figure 4a). Results for three stations on
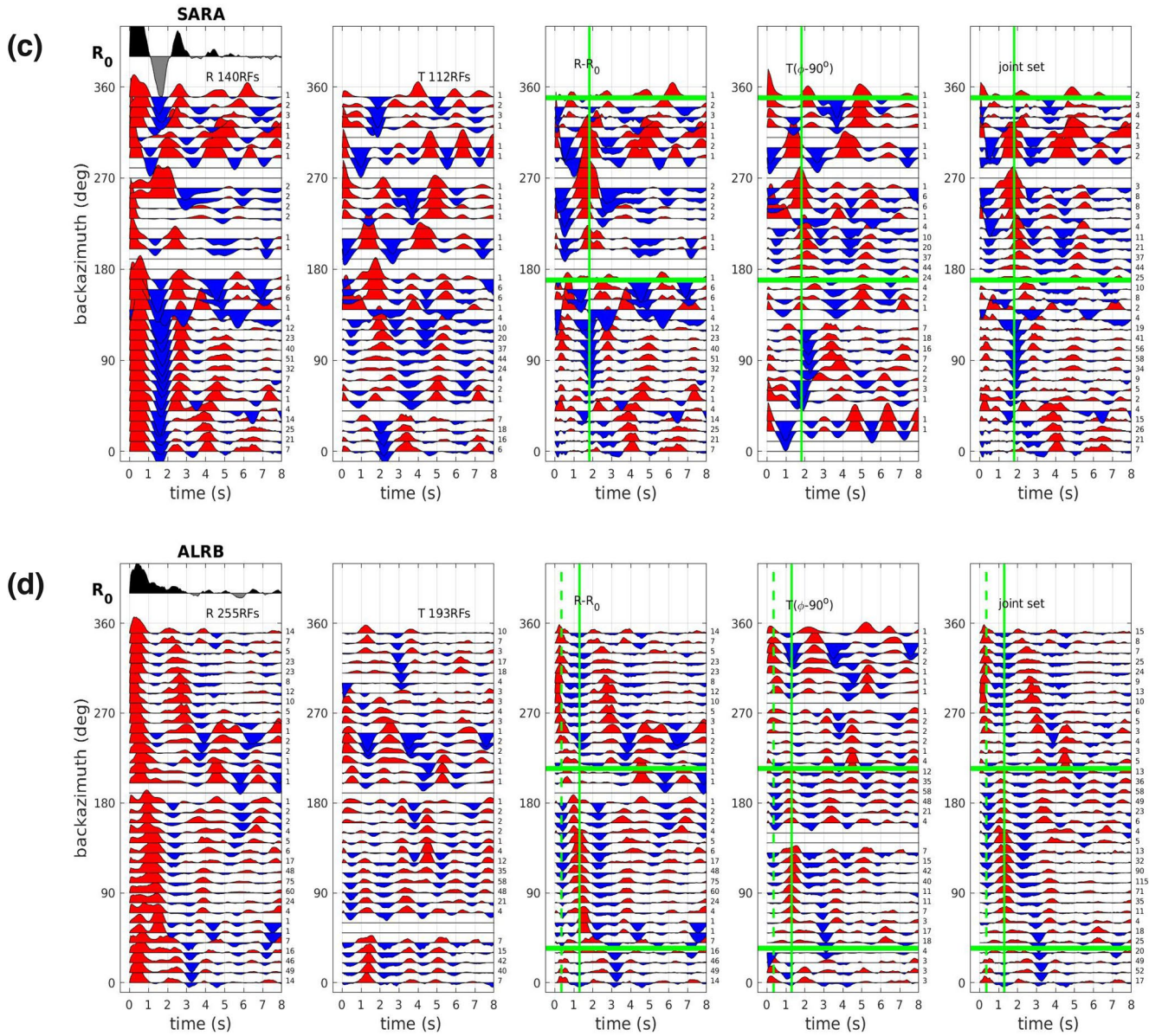
Figure 3. (Continued)

Timor (NOMU and TL07) and Savu (SAVU) islands have a value larger than 50% and will be analyzed in detail (Section 4).

Figures 2 and 3 and Figures S1–S5 in Supporting Information S1 present the RF waveforms in five panels for each station, where the interpreted A1 arrivals are outlined. In general, we find that the converted energy on tangential components is strong and coherent (second panels for each station plot). Many tangential conversions present comparable amplitude to the radial RFs as shown in the first and second panels for each station plot. We also observe a clear 360° periodic change from red positive signals to blue negative signals over backazimuth (i.e., polarity reversal) on both raw radial and tangential components (first and second panels). These polarity-reversal arrivals are stacked down in the standard station average of the radial RFs (R_0 in the first panels). The processed components in the third and fourth panels present consistent polarities for those isolated A1 signals outlined by vertical green lines. In each station plot, the processed components and the joint set from the third to fifth panels effectively highlight the dominant A1 signal at each station. More than half of the stations present a single A1 peak arrival that stands out in the waveforms. We also identified two A1 arrivals for a few stations
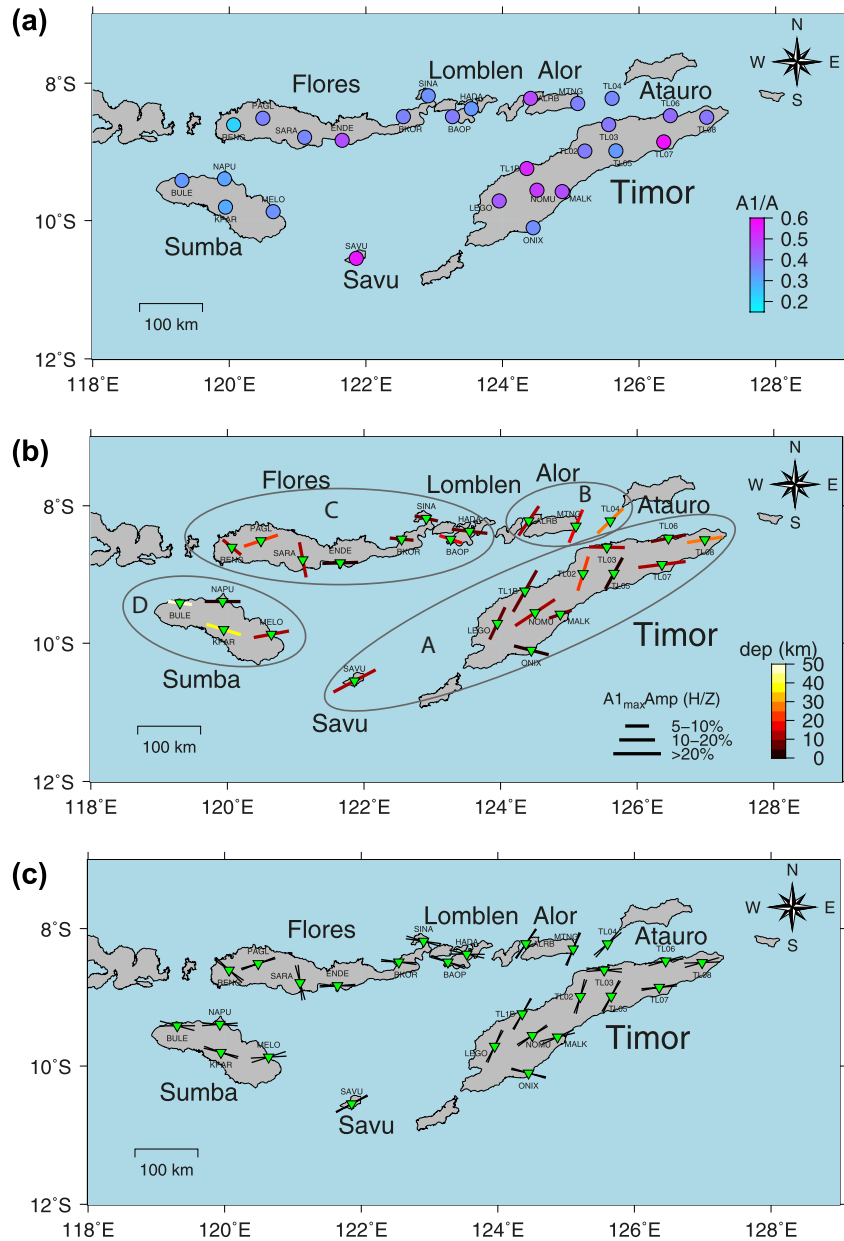
Figure 4. (a) Receiver function (RF) amplitude in the first azimuthal harmonic (A1) as a fraction of the total RF signal amplitude for all stations, averaged between 0 and 8 s. (b) Interpreted peak A1 arrivals at each station (green inverted triangles) where the bootstrapping uncertainty is less than 60% of the A1-arrival amplitude. The color of the bar represents the inferred depth of the signal. Bar orientation corresponds to the structural strike revealed by the $A1_{max}$ signal. Bar length represents amplitude of the arrival. (c) Strike uncertainties from bootstrapping for $A1_{max}$ signals presented in panel (b). Two black sticks for each station are the maximum and minimum strike values from bootstrapping and the difference marks an estimated uncertainty.

(e.g., Figure 2, Figure S1 in Supporting Information S1) that are representative and discussed in the next section. Generally, most of these strong A1 arrivals are detected within the first 4 s. Six stations on the outer arc islands of Timor and Savu (Figures S1 and S2 in Supporting Information S1) and 5 stations on inner arc islands of east Flores and Lomblen (Figure S3 in Supporting Information S1) have their strongest A1 energy in early arrivals within the first 2 s.

For those stations with multiple peaks in the A1-harmonic solution at different times/depths, the maximum A1 amplitude solution (hereafter referred to as $A1_{max}$) is presumed to be the best-constrained arrival (Schulte-Pelkum,

Caine, et al., 2020; Schulte-Pelkum, Ross, et al., 2020). In Figure 4b, we present the $A1_{max}$ arrivals with their strike (shown by bar orientations) and depth (shown by bar colors) in a map view, visualizing the distribution of the most dominant A1 conversions in both lateral and vertical content. Most $A1_{max}$ arrivals are concentrated in the depth range above 35 km. The uncertainties of these RF strikes are presented in Figure 4c, showing that the bootstrap strike errors of the $A1_{max}$ signals are small, with values lower than 10°.

4. Discussion

We find many large-amplitude A1 arrivals in RF waveforms (Figures 2 and 3, Figures S1–S5 in Supporting Information S1) and high integrated A1 energy (>30%) within the first 8 s (Figure 4a) at most of the stations. These observations indicate the pervasive presence of dipping and/or anisotropic fabrics across the entire collisional zone. $A1_{max}$ signals generated by these dominant oriented structures appear to concentrate in the crustal depth range (<35 km) for most stations (Figure 4b). In general, the cumulative A1 energy is higher in the east compared to the west (Figure 4a). By examining A1 signals and RF waveforms for individual stations (Figures 2 and 3, Figures S1–S5 in Supporting Information S1), we observe large differences between stations on the inner and outer arc islands (e.g., comparing Figure 2 with Figure 3). Changes in A1 signals for stations in different segments of the volcanic arc (Figure 3) and in different orogenic islands in the outer arc (Figures S1–S5 in Supporting Information S1) are also distinct. More interestingly, we recognize clear regional patterns in terms of the strikes from the $A1_{max}$ signals as we show in Figure 4b. Together with existing knowledge of the crustal velocity structures by Zhang and Miller (2021) and inferences from the literature detailing geology and volcanism (e.g., Harris, 2011; Harris et al., 2009; Kaneko et al., 2007; Muraoka et al., 2002a), we cluster these RF results into four different areas (gray ellipses in Figure 4b). They are referred to as Zone A, B, C, and D hereafter, which are used to guide the discussion in this section. Besides the $A1_{max}$ arrival, some strong and interpretable additional A1 arrivals for a few stations are collectively considered in the discussion (e.g., Figure 2). Here, we only introduce representative stations in each zone that provide good examples of signal complexity in our data set.

Zone A includes Savu and Timor in the outer arc (Figure 4b), where the cumulative energy of A1 signals is relatively high (Figure 4a). These areas are also generally characterized by relatively slow Vs materials in the crust, contrasting with the faster Vs materials revealed beneath the inner arc islands and the outer arc island of Sumba (Zhang & Miller, 2021). In Zone A, the strikes of the $A1_{max}$ signals can be further categorized into two clusters. One (~NE-SW-oriented) is roughly sub-parallel to the orientation of islands of Timor and Savu that is also the orogenic strike determined from surface structural mapping (Harris, 2011; Kaneko et al., 2007). This orientation is roughly parallel to the Timor Trough. Hereafter, we refer to the RF strike of this cluster as orogen-parallel strike. The other ~NNE-SSW oriented strike group is roughly sub-parallel to the plate convergence direction documented by the plate motion vector (DeMets et al., 1994) and recent GPS velocity field study (Figures 1a and 4b; Koulali et al., 2016). The plate convergence direction differs from the strike of the Timor Trough and orogenesis of the outer arc islands (Figures 1a and 4b). Hereafter, we refer to this orientation as convergence-parallel strike.

Zone B includes three stations on the extinct portion of the inner arc on the Alor and Atauro islands north of East Timor (Figure 4b). We group the other stations on the islands of Flores and Lomblen that accommodate active volcanism as Zone C (Figure 4b). Although both areas are part of the inner arc, the RF waveforms, A1 signals, and $A1_{max}$-inferred strikes in Zone B exhibit a dramatic difference to those of stations in Zone C within the active arc segment (Figures 3 and 4b, Figures S3–S4 in Supporting Information S1). The $A1_{max}$-inferred strikes in Zone B are oriented ~NNE-SSW, whereas the strikes in Zone C are mostly in ~E-W orientations with an exception of station SARA (Figure 4b).

Lastly, we group results from the four stations on Sumba island as a separate Zone D (Figure 4b). The roughly E-W strike pattern from four stations in Zone D is generally aligned with the orogenic strikes in Sumba but the depths of the dominant oriented structures beneath different stations are variable (Figures 4b, Figure S5 in Supporting Information S1). It is obvious that the orientations are different from the results in Zone A although they are both parts of outer arc islands. Sumba island has unusual morphology, geology, volcanism, and lacks strong compressional deformation (e.g., Abdullah et al., 2000; Audley-Charles, 1985; Lytwyn et al., 2001; Rutherford et al., 2001), in contrast to Savu and Timor that are dominated by recent orogenesis under compressional deformation (e.g., Harris, 2011). Therefore, we interpret the newly imaged structures in Zone D to be
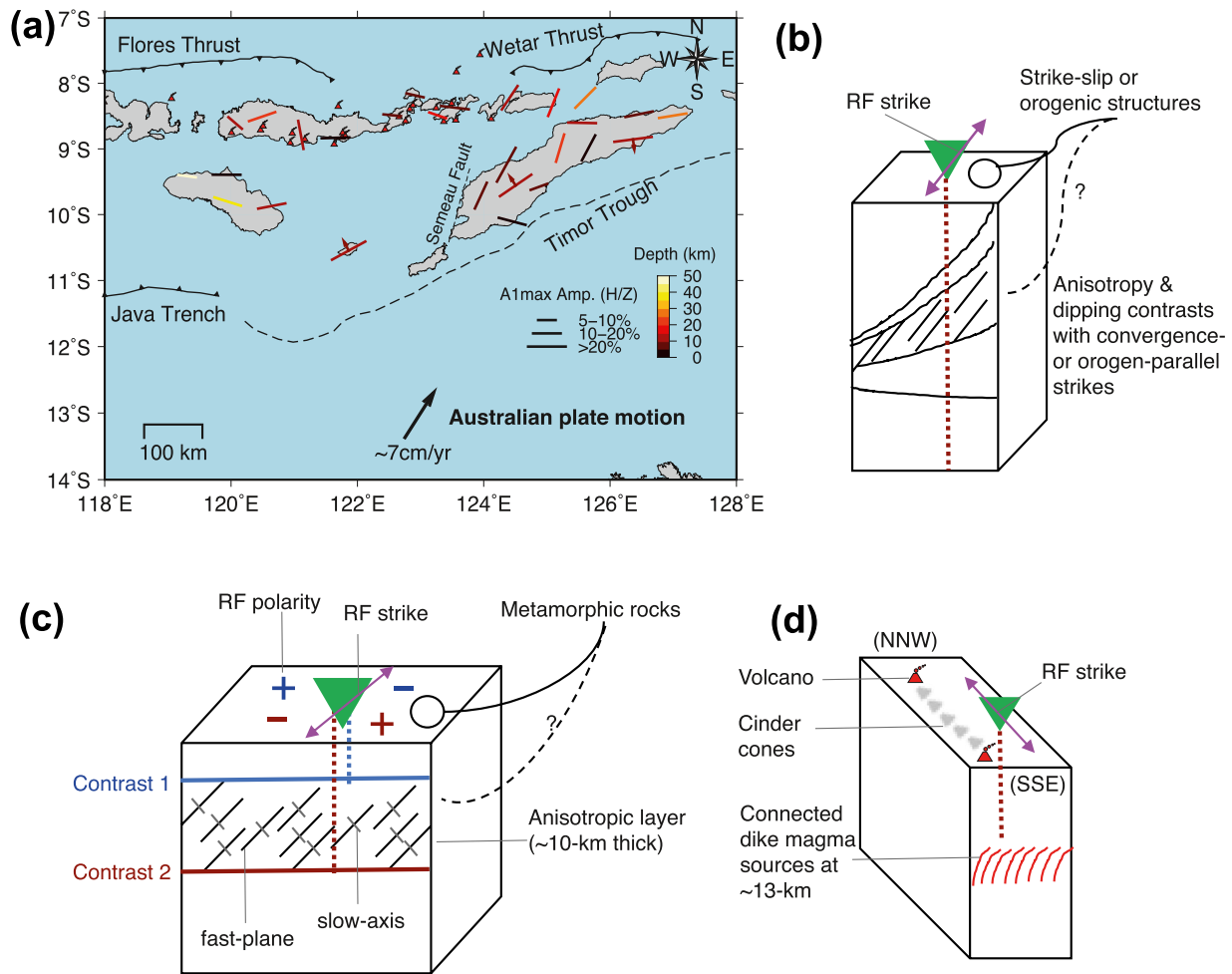
Figure 5. Interpretation of receiver function results. (a) A summary of interpreted A1 peak arrivals (as in Figure 4b) and tectonic features (as in Figure 1). Semau fault is denoted by the thin dashed line, after Kaneko et al. (2007). (b) Schematic illustration of the oriented fabrics (showing a composite of dipping boundaries and rock deformation fabrics) with convergence- and orogen-parallel strikes interpreted on Timor and Alor islands in Zone A. (c) Schematic illustration of the anisotropic structures revealed by a pair of polarity-reversal signals with opposite polarity observed at stations NOMU, SAVU, and TL07, which are likely linked to metamorphic rocks. The black long lines are fast planes and the gray short lines are slow-axis that are perpendicular to it. (d) Schematic illustration of the volcanic fabrics associated with connected dike magma sources beneath station SARA in Flores. Green reversed triangles on top of the cubes mark seismic stations. Dashed vertical lines beneath stations represent interpreted A1 signals generated by the oriented structures with strikes shown as magenta bars.

associated with the distinct tectonics on Sumba, different from those found on Savu and Timor in Zone A that are mostly interpreted to be orogenic and strike-slip structures resulting from crustal shortening and plate convergence (discussed in the next paragraph). For example, station NAPU presents an E-W oriented fabric strike in the shallow (~3 km) crust near the surface (Figure 4b, Figure S5 in Supporting Information S1). It is well-known that the surface to the north of the station is covered by Pleistocene age reef terraces that have been uplifted in the Quaternary, whereas to the south the Middle to Upper Miocene rocks primarily have an extensional tectonic regime (Fleury et al., 2009). Therefore, our observation from the station NAPU is likely to be associated with a deeply buried portion of the structural boundary separating these two domains.

The oriented fabrics imaged in Zone A are dominated by orogen-parallel and convergent-parallel strikes (Figure 4b). Orientation correlation between those orogen-parallel fabrics with the orogenic strike of the mountain belt suggests that orogenesis is likely the major control forming these structures at shallow-to-middle crustal depths. Meanwhile, geologic observations have documented a number of NNE-SSW or NE-SW trending strike-slip faults that are part of shear systems in both East (Benincasa et al., 2012; Duffy et al., 2013) and West Timor (Charlton et al., 1991). A major NNE-SSW trending left-lateral strike-slip fault, called the Semau fault, is also mapped offshore west of Timor (Figure 5a; Kaneko et al., 2007) but it is relatively poorly constrained. The

imaged structures in Zone A present two dominant strikes that are roughly consistent with the orientations of the local structures mapped in the field. Such correlation suggests that many fabrics imaged on Timor, in particular for those with convergence-parallel strikes, might be related to the strike-slip structures as illustrated in Figure 5b. GPS observations and field mapping have also inferred that Timor has accommodated a very large amount of coupling to the Australian plate (63%) and significant crustal shortening in comparison to areas to the west of Semau fault (with 21%–41% coupling; Harris, 2011; Nugroho et al., 2009; Tate et al., 2015). Together with observation of the volcanism cessation to the north of Timor, the area has been considered to accommodate the most advanced stage of collision (e.g., Harris, 2011). Zone A, in this study, has very high cumulative A1 energy compared to the west (Figure 4a). Therefore, we suggest some orogen-parallel fabrics are part of the orogenic structures that result from the crustal shortening and mountain building in response to the very advanced arc-continent collision. Taken together, we propose the tectonic fabrics imaged in Zone A support the interpretation that Timor not only accommodates an advanced collision between Banda Arc with the Australian margin, but also shows strike-slip motion generated by the overall NNE convergence direction of the Australian plate with respect to the Eurasian plate. Our observations, in this case, provide new deep structural evidence that links the inferences from other deformation-related observations from geology and geodesy.

In Zone A, there are three representative stations on Timor (NOMU and TL07) and Savu (SAVU) islands at which we observe a pair of polarity-reversal arrivals that dominate the energy in RFs within the first 2 s (Figures 2 and 4, Figure S1 in Supporting Information S1). These three stations show that >50% of the RF energy is found in the first azimuthal harmonic (Figure 4a) and the strikes of the $A1_{max}$ signals align with the island orientation and the orogenic strike (Figure 4b). For example, station NOMU, located in the central part of West Timor (Figure 4b), has the $A1_{max}$ arrival at 1.65 s but there is another strong A1 signal at 0.65 s (Figure 2). Intriguingly, for these two arrivals, the polarity flips at a similar backazimuth (~56° and –236° marked by horizontal green lines in Figures 2c–2e) but with an opposite polarity (Figures 2c–2e). For the earlier arrival at 0.65 s, seismic waves emerging from the northwest (backazimuth in 0°–56° and 236°–360°) create a positive polarity conversion, whereas waves emerging from the southeast (56°–236° backazimuth) create a negative polarity conversion. In contrast, for the latter arrival at 1.65 s, conversions from the northwest and the southeast have negative and positive polarities, respectively. Similar double polarity-reversal arrivals with opposite polarity are observed for station SAVU on the outer arc island of Savu (at 0.47 s and 1.53 s with a strike of 62° or 242°) and station TL07 (at 0.65 s and 1.65 s with a strike of 83° or 263°) in the southern coast of East Timor (Figure S1 in Supporting Information S1). These signals are inferred to be from a similar depth range (<11 km) in the shallow crust for all three stations. However, the polarities in both arrivals are the opposite between station TL07 and the other two stations (Figure S1 in Supporting Information S1).

Both dipping layers and anisotropy should be considered in terms of interpreting the A1 arrivals. Yet, on the raw tangential components of these three stations, we do not observe a preceding arrival at zero time with periodic polarity reversal (Figures 2f, Figure S1 in Supporting Information S1) that would indicate the presence of an individual dipping layer (e.g., Levin & Park, 1998; Schulte-Pelkum & Mahan, 2014a). Therefore, we favor anisotropy as the cause to explain our RF observation. In addition, metamorphic rocks that are seismically anisotropic are exposed on the surface throughout the Timor and Savu islands (Harris et al., 2009; Kaneko et al., 2007). In central West Timor, the Mutis Complex is located near station NOMU, which consists of high P/T metamorphic schists and gneisses (Kaneko et al., 2007). Exposures of metamorphic rocks are also documented near station SAVU in the central part of Savu (Harris et al., 2009). In East Timor, the surface exposures of rocks near station TL07 along the southern coast are primarily sedimentary rocks (Kaneko et al., 2007). However, there are metamorphic rocks mapped along the north coast that are interpreted to extend southward with metamorphic grade dropping sharply from north to south (Kaneko et al., 2007). Our new observations, in this case, raise the possibility that the metamorphic rocks mapped at the surface extend throughout the subsurface and are representative of the structural elements of the shallow crust beneath these stations (Figure 5c). Furthermore, we interpret the observed double polarity reversal arrivals with opposite polarity as conversions originating from the top and bottom boundaries of a ~10-km thick anisotropic layer with a symmetry (slow) axis dipping toward the northwest for station NOMU and SAVU and toward the southeast for station TL07 (Figure 5c).

An intriguing observation is that the strikes from three stations on the inner arc islands of Alor (ALRB and MTNG) and Atauro (TL04) in Zone B appear to be consistent with convergence-parallel oriented fabrics imaged on the outer arc islands in Zone A. In the study region, it has been proposed that the distribution of strain is away

from the Timor Trough deformation front and partitioned into fore-arc and backarc thrusts, strike-slip faults, and orogenic structures (Koulali et al., 2016; Nugroho et al., 2009). Backarc thrusts (Wetar and Flores Thrusts in Figures 1a and 5a) are identified by offshore seismic reflection profiles (Silver et al., 1983). Focal mechanisms from large earthquakes also support that active southward thrusting in the backarc is ongoing (e.g., McCaffrey, 1988). In Timor, the fabrics imaged in Zone A support the occurrence of strike-slip and orogenic structures with convergence-parallel and orogen-parallel orientations. The NNE-SSW strikes identified in this study, which are parallel with GPS velocity field and plate motion direction, are only observed on the islands of Timor, Alor, and Atauro (Figures 4b and 5). The RF waveforms from stations in Zone B also share more similarities to those in Zone A (as outer arc) instead of Zone C (as inner arc). Therefore, we interpret the NNE-SSW-oriented fabrics imaged in Zone B to be associated with strike-slip structures that probably also contribute to the strain partitioning together with those strike-slip structures found in Zone A. Koulali et al. (2016) proposed that the strain is transferred from Timor Trough to backarc thrusts via a series of NNE-SSW trending left-lateral strike-slip faults offshore west of Timor and Alor, based on GPS observations and kinematic modeling. However, these offshore faults are fairly poorly constrained due to a lack of data. There is also a massive topographic change in the strait channel (~20 km-wide) between the Timor and Atauro, which is being considered as a plate boundary by many studies (e.g., Keep & Haig, 2010). Therefore, it is not clear how these strike-slip faults are connected offshore. In this study, we observe the correlation of Zone A and Zone B in terms of structural orientations. To our knowledge, this is the first tentative evidence for crustal structural similarities between the outer and inner arcs. However, further investigation is required to fully address the mechanism of strain transfer from the Timor Trough to backarc thrusts.

In Zone C, we interpret the RF strikes (Figure 4b) and waveform characteristics (Figure 3, Figure S3 in Supporting Information S1) to be closely associated with the different magmatic systems along the arc. For station RENG at the western end of Flores Island, the cumulative A1 energy (23%; Figure 4a), the A1 signal amplitude (Figure 3), and the tangential component energy (the second panel for the station in Figure 3a) are small. There is a caldera lake nearby but with no historical eruptions. Station PAGL on West Flores presents a dominant $A1_{max}$ signal at 2.88 s (~24 km in depth) with a strike of ~72° or ~252° that is roughly parallel to the WSW-ENE anticline axis of volcanic basement units to its south (Figures 1, 3 and 4), where there are a poorly studied caldera and a new lava dome. The remaining three stations (ENDE, BKOR, and SINA) on eastern Flores all have their strongest A1 energy at early times of less than 1 s (Figure S3 in Supporting Information S1), suggesting the presence of structures with ~E-W orientations near the surface (<~4–6 km). The RF waveforms of station HADA on Lomblen island are the most complicated example, where several sets of strong periodic signals are clearly visible in the waveforms (Figure S3 in Supporting Information S1). Lewotolo volcano located ~12 km away is the only currently actively erupting volcano in the region. Therefore, active magmatic structures might influence the observed complicated conversions. The other station (BAOP) on SW Lomblen island presents rather simple waveforms and azimuthal variations are found in earlier arrivals (Figure S3 in Supporting Information S1). The nearest volcano has not had any historical eruptions. Regardless of these differences, both stations on Lomblen island reveal similar ~E-W structural strikes to that observed on the eastern Flores.

Station SARA in central-western Flores in Zone C has a near NNW-SSE orientation of the $A1_{max}$ signal at 1.82 s (at depth of ~13 km), contrasting with the rest of the stations that generally strike ~E-W on both sides (Figures 4b and 5a). About 15-to-20-km west of the station, there are at least 78 cinder cones aligned 20 km along an ~NNW-SSE trending rift zone, known as the Bajawa rift and Cinder Cone Complex (Muraoka et al., 2002a). Most fractures and folding axes mapped on the surface are also close to the NNW-SSE direction (Muraoka et al., 2002a). In this case, the inferred fabric strike (169° or 349°) beneath station SARA is consistent with the surface structural alignment. In addition, volcanic rocks of the Bajawa area are very homogeneous in composition across their spatial extent, which indicates a connected dike and magma chamber system at depth resulting in these aligned cones (Muraoka et al., 2002a; Muraoka et al., 2002b). Phase relations from rock samples also indicate a possible shallow magma source at a depth of ~10 km (Muraoka et al., 2002b). The oriented structure observed for station SARA is located at a depth of ~13 km, which is compatible with the depth inferred from rock phase relation. Taken together, we interpret the oriented fabric beneath station SARA to be associated with this connected dike magmatic system (Figure 5d).

Interestingly, in Zone C, the strikes of the $A1_{max}$ arrivals from a few stations (e.g., RENG, PAGL, and SARA) appear to be tangential to the volcanic edifices in their vicinity (Figure 5a). These observations might indicate

deep crustal structures or fabrics that are concentric to the volcanic edifices, which are also observed at a number of arc volcanoes in Alaska (Schulte-Pelkum, Caine, et al., 2020). The polarity-reversed arrivals observed in this study also provide a hint that these volcanic edifices might be more complex than a single, concentric low-velocity magma chamber. However, further analysis is currently hindered due to the absence of dense array data sets from local seismographic networks surrounding the volcanoes, similar to that of the Alaska Volcano Observatory (https://avo.alaska.edu). Although no conclusive interpretation of the volcanic structures is presented here due to the scope of the study, our results suggest potential correlations between RF observations with arc volcanism. In addition, the observed fabrics in East Flores and Lomblen islands are mostly E-W oriented in the shallow crust, where the volcanism has been recently active in comparison to the West Flores. For a similar volcanic arc setting in Northern Japan, Bianchi et al. (2015) observe variable RF orientations in the shallow crust and conclude that the vicinity of active volcanic edifices might change the local conditions and therefore induce a ductile deformation, leading to local structural patterns. The regional strike pattern we observe here could motivate denser data coverage to enable future seismic studies of arc volcano evolution.

5. Conclusions

This study analyzed ∼5 years' (2014–2019) radial and tangential teleseismic RFs observed at 30 temporary seismic stations installed in one of the most complicated regions on the planet—the Banda Arc-Australian continent collisional zone. We observed azimuthal variations and polarity reversal in the RFs, which are indicative of the presence of tectonic fabrics (dipping and/or anisotropic structures) in the crust across the entire collision zone. We observed regional patterns in terms of RF waveform characteristics and distribution of the dominant oriented fabrics. We also identified very intriguing spatial correlations of these patterns with geology, metamorphic rocks, orogenic structures, strike-slip structures, and volcanic activities. Our data adds a much-needed subsurface element to complement surface observations, therefore improves our general understanding of this region in terms of orogenesis, volcanism, strain partitioning, arc-continent collision, and plate convergence. However, we acknowledge that the interpreted models presented herein are not unique. In particular, it is difficult to determine the exact source of the imaged fabrics below the surface in such a complex convergent boundary.

Our new RF observations are helpful to address the inherent ambiguity of depth-integrated seismic azimuthal anisotropy analyses, such as shear wave (S/SKS/SKKS) splitting (Harris & Miller, in press) and surface wave anisotropy inversion, which are both ongoing projects resulting from the Banda Arc seismic experiment. It also contributes to the interpretation and modeling of geodetic GPS measurements that are indicative of lithosphere and slab deformation. In addition, it provides a new perspective in understanding the depth and extent of the strike-slip faults and shear systems, metamorphic rocks, orogenic and volcanic structures, complement surface observations. The imaged fabrics are informative for active structures that are subject to earthquake and volcanic hazards.

Data Availability Statement

The facilities of the Australian Passive Seismic Server (AusPass) and of the Incorporated Research Institutions for Seismology (IRIS) were used for access to waveforms and related metadata of the YS network (https://doi.org/10.7914/SN/YS_2014) as well as the earthquake catalog used in this study. Data were retrieved via the SOD program (Owens et al., 2004; http://www.seis.sc.edu/sod) and Fetch scripts (https://seiscode.iris.washington.edu/projects/ws-fetch-scripts). The Taup Toolkit, Seismic Analysis Code (SAC) and Computer Programs in Seismology (CPS; Herrmann, 2013) packages were used for travel time calculation, data preprocessing, and computing receiver function. Global Volcanism Program, Smithsonian Institution (2013) was used to access information describing volcanoes and eruptive activities.

References

Abdullah, C. I., Rampnoux, J. P., Bellon, H., Maury, R. C., & Soeria-Atmadja, R. (2000). The evolution of Sumba Island (Indonesia) revisited in the light of new data on the geochronology and geochemistry of the magmatic rocks. *Journal of Asian Earth Sciences*, *18*(5), 533–546. https://doi.org/10.1016/S1367-9120(99)00082-6

Audet, P. (2015). Layered crustal anisotropy around the San Andreas fault near Parkfield, California. *Journal of Geophysical Research: Solid Earth*, *120*(5), 3527–3543. https://doi.org/10.1002/2014JB011821

Audley-Charles, M. G. (1985). The Sumba enigma: Is Sumba a diapiric fore-arc nappe in process of formation? *Tectonophysics*, *119*(1–4), 435–449. https://doi.org/10.1016/0040-1951(85)90049-6

Audley-Charles, M. G. (2004). Ocean trench blocked and obliterated by Banda forearc collision with Australian proximal continental slope. *Tectonophysics*, *389*(1–2), 65–79. https://doi.org/10.1016/j.tecto.2004.07.048

Bar, N., Long, M. D., Wagner, L. S., Beck, S. L., & Tavera, H. (2019). Receiver function analysis reveals layered anisotropy in the crust and upper mantle beneath southern Peru and northern Bolivia. *Tectonophysics*, *753*, 93–110. https://doi.org/10.1016/j.tecto.2019.01.007

Benincasa, A., Keep, M., & Haig, D. W. (2012). A restraining bend in a young collisional margin: Mount Mundo Perdido, East Timor. *Australian Journal of Earth Sciences*, *59*(6), 859–876. https://doi.org/10.1080/08120099.2012.686453

Bianchi, I., Bokelmann, G., & Shiomi, K. (2015). Crustal anisotropy across northern Japan from receiver functions. *Journal of Geophysical Research: Solid Earth*, *120*(7), 4998–5012. https://doi.org/10.1002/2014JB011681

Birkey, A., Ford, H. A., Dabney, P., & Goldhagen, G. (2021). The lithospheric architecture of Australia from seismic receiver functions. *Journal of Geophysical Research: Solid Earth*, *126*(4), e2020JB020999. https://doi.org/10.1029/2020JB020999

Bourke, J., Levin, V., Linkimer, L., & Arroyo, I. (2020). A recent tear in subducting plate explains seismicity and upper mantle structure of southern Costa Rica. *Geochemistry, Geophysics, Geosystems*, *21*(12), e2020GC009300. https://doi.org/10.1029/2020GC009300

Charlton, T. R., Barber, A. J., & Barkham, S. T. (1991). The structural evolution of the Timor collision complex, eastern Indonesia. *Journal of Structural Geology*, *13*(5), 489–500. https://doi.org/10.1016/0191-8141(91)90039-L

Chen, X., Park, J., & Levin, V. (2021). Anisotropic layering and seismic body waves: Deformation gradients, initial S-polarizations, and converted-wave birefringence. *Pure and Applied Geophysics*, *1–23*(6), 2001–2023. https://doi.org/10.1007/s00024-021-02755-6

DeMets, C., Gordon, R. G., Argus, D. F., & Stein, S. (1994). Effect of recent revisions to the geomagnetic reversal time scale on estimates of current plate motions. *Geophysical Research Letters*, *21*(20), 2191–2194. https://doi.org/10.1029/94GL02118

Duffy, B., Quigley, M., Harris, R., & Ring, U. (2013). Arc-parallel extrusion of the Timor sector of the Banda Arc-continent collision. *Tectonics*, *32*(3), 641–660. https://doi.org/10.1002/tect.20048

Elburg, M. A., Foden, J. D., Van Bergen, M. J., & Zulkarnain, I. (2005). Australia and Indonesia in collision: Geochemical sources of magmatism. *Journal of Volcanology and Geothermal Research*, *140*(1–3), 25–47. https://doi.org/10.1016/j.jvolgeores.2004.07.014

Elburg, M. A., Van Bergen, M. J., & Foden, J. D. (2004). Subducted upper and lower continental crust contributes to magmatism in the collision sector of the Sunda-Banda Arc, Indonesia. *Geology*, *32*(1), 41–44. https://doi.org/10.1130/G19941.1

Fainstein, R., do Rosário, J. D. D. C., Guterres, H. C., dos Reis, R. P., & da Costa, L. T. (2020). Coastal and offshore provinces of Timor-Leste—Geophysics exploration and drilling. *The Leading Edge*, *39*(8), 543–550. https://doi.org/10.1190/tle39080543.1

Fichtner, A., De Wit, M., & van Bergen, M. (2010). Subduction of continental lithosphere in the Banda Sea region: Combining evidence from full waveform tomography and isotope ratios. *Earth and Planetary Science Letters*, *297*(3–4), 405–412. https://doi.org/10.1016/j.epsl.2010.06.042

Fleury, J. M., Pubellier, M., & de Urreiztieta, M. (2009). Structural expression of forearc crust uplift due to subducting asperity. *Lithos*, *113*(1–2), 318–330. https://doi.org/10.1016/j.lithos.2009.07.007

Frothingham, M. G., Mahan, K. H., Schulte-Pelkum, V., Caine, J. S., & Vollmer, F. W. (2022). From crystals to crustal-scale seismic anisotropy: Bridging the gap between rocks and seismic studies with digital geologic map data in Colorado. *Tectonics*, *41*(1), e2021TC006893. https://doi.org/10.1029/2021TC006893

Global Volcanism Program. (2013). Volcanoes of the world, v. 4.10.2 (24 Aug 2021) In E. Venzke, (Ed.). Smithsonian Institution. https://doi.org/10.5479/si.GVP.VOTW4-2013

Gosselin, J. M., Audet, P., Fry, B., & Warren-Smith, E. (2021). Seismic constraint on heterogeneous deformation and stress state in the forearc of the Hikurangi subduction zone, New Zealand. *The Seismic Record*, *1*(3), 145–153. https://doi.org/10.1785/0320210032

Haig, D. W., & McCartain, E. (2007). Carbonate pelagites in the post-Gondwana succession (Cretaceous–Neogene) of East Timor. *Australian Journal of Earth Sciences*, *54*(6), 875–897. https://doi.org/10.1080/08120090701392739

Hall, R. (2017). Southeast Asia: New views of the geology of the Malay Archipelago. *Annual Review of Earth and Planetary Sciences*, *45*(1), 331–358. https://doi.org/10.1146/annurev-earth-063016-020633

Harris, C. W., & Miller, M. S. (in press). Mantle flow deflected by arc-continent collision and continental subduction in eastern Indonesia. *Seismology Research Letter*. https://doi.org/10.1785/0220210281

Harris, C. W., Miller, M. S., Supendi, P., & Widiyantoro, S. (2020). Subducted lithospheric boundary tomographically imaged beneath arc-continent collision in eastern Indonesia. *Journal of Geophysical Research: Solid Earth*, *125*(8), e2019JB018854. https://doi.org/10.1029/2019JB018854

Harris, R. (2011). The nature of the Banda Arc–continent collision in the Timor-region. In D. Brown & P. D. Ryan (Eds.), *Arc–Continent Collision, Frontiers in Earth Sciences* (pp. 163–211). Springer. https://doi.org/10.1007/978-3-540-88558-0_7

Harris, R., Vorkink, M. W., Prasetyadi, C., Zobell, E., Roosmawati, N., & Apthorpe, M. (2009). Transition from subduction to arc-continent collision: Geologic and neotectonic evolution of Savu Island, Indonesia. *Geosphere*, *5*(3), 152–171. https://doi.org/10.1130/GES00209.1

Herrmann, R. B. (2013). Computer programs in seismology: An evolving tool for instruction and research. *Seismology Research Letter*, *84*(6), 1081–1088. https://doi.org/10.1785/0220110096

Hilton, D. R., Hoogewerff, J. A., Van Bergen, M. J., & Hammerschmidt, K. (1992). Mapping magma sources in the east Sunda-Banda arcs, Indonesia: Constraints from helium isotopes. *Geochimica et Cosmochimica Acta*, *56*(2), 851–859. https://doi.org/10.1016/0016-7037(92)90105-R

Honthaas, C., Réhault, J. P., Maury, R. C., Bellon, H., Hémond, C., Malod, J. A., et al. (1998). A Neogene back-arc origin for the Banda Sea basins: Geochemical and geochronological constraints from the Banda ridges (East Indonesia). *Tectonophysics*, *298*(4), 297–317. https://doi.org/10.1016/S0040-1951(98)00190-5

Jiang, C., Zhang, P., White, M. C., Pickle, R., & Miller, M. S. (2022). A detailed earthquake catalog for Banda Arc–Australian plate collision zone using machine-learning phase picker and an automated workflow. *The Seismic Record*, *2*(1), 1–10. https://doi.org/10.1785/0320210041

Kaneko, Y., Maruyama, S., Kadarusman, A., Ota, T., Ishikawa, M., Tsujimori, T., et al. (2007). On-going orogeny in the outer-arc of the Timor–Tanimbar region, eastern Indonesia. *Gondwana Research*, *11*(1–2), 218–233. https://doi.org/10.1016/j.gr.2006.04.013

Keep, M., & Haig, D. W. (2010). Deformation and exhumation in Timor: Distinct stages of a young orogeny. *Tectonophysics*, *483*(1–2), 93–111. https://doi.org/10.1016/j.tecto.2009.11.018

Kennett, B. L. N., & Engdahl, E. R. (1991). Traveltimes for global earthquake location and phase identification. *Geophysical Journal International*, *105*(2), 429–465. https://doi.org/10.1111/j.1365-246X.1991.tb06724.x

Koulali, A., Susilo, S., McClusky, S., Meilano, I., Cummins, P., Tregoning, P., et al. (2016). Crustal strain partitioning and the associated earthquake hazard in the eastern Sunda-Banda Arc. *Geophysical Research Letters*, *43*(5), 1943–1949. https://doi.org/10.1002/2016GL067941

Levin, V., Elkington, S., Bourke, J., Arroyo, I., & Linkimer, L. (2021). Seismic anisotropy in southern Costa Rica confirms upper mantle flow from the Pacific to the Caribbean. *Geology*, *49*(1), 8–12. https://doi.org/10.1130/G47826.1

Levin, V., & Park, J. (1998). P-SH conversions in layered media with hexagonally symmetric anisotropy: A CookBook. *Pure and Applied Geophysics*, *151*, 669–697. https://doi.org/10.1007/978-3-0348-8777-9_25

Ligorría, J. P., & Ammon, C. J. (1999). Iterative deconvolution and receiver-function estimation. *Bulletin of the Seismological Society of America*, *89*(5), 1395–1400. https://doi.org/10.1785/BSSA0890051395

Lytwyn, J., Rutherford, E., Burke, K., & Xia, C. (2001). The geochemistry of volcanic, plutonic and turbiditic rocks from Sumba, Indonesia. *Journal of Asian Earth Sciences*, *19*(4), 481–500. https://doi.org/10.1016/S1367-9120(00)00031-6

McCaffrey, R. (1988). Active tectonics of the eastern Sunda and Banda arcs. *Journal of Geophysical Research*, *93*(B12), 15163–15182. https://doi.org/10.1029/JB093iB12p15163

Miller, M. S. (2014). *Transitions in the Banda Arc-Australia continental collision* [Dataset]. Seismic Network, International Federation of Digital Seismograph Networks. https://doi.org/10.7914/SN/YS_2014

Miller, M. S., O'Driscoll, L. J., Roosmawati, N., Harris, C. W., Porritt, R. W., Widiyantoro, S., et al. (2016). Banda Arc experiment—Transitions in the Banda Arc–Australian continental collision. *Seismological Research Letters*, *87*(6), 1417–1423. https://doi.org/10.1785/0220160124

Miller, M. S., Zhang, P., Dahlquist, M. P., West, A. J., Becker, T. W., & Harris, C. W. (2021). Inherited lithospheric structures control arc-continent collisional heterogeneity. *Geology*, *49*(6), 652–656. https://doi.org/10.1130/G48246.1

Müller, R. D., Sdrolias, M., Gaina, C., & Roest, W. R. (2008). Age, spreading rates, and spreading asymmetry of the world's ocean crust. *Geochemistry, Geophysics, Geosystems*, *9*(4), Q04006. https://doi.org/10.1029/2007GC001743

Muraoka, H., Nasution, A., Urai, M., Takahashi, M., Takashima, I., Simanjuntak, J., et al. (2002a). Tectonic, volcanic and stratigraphic geology of the Bajawa geothermal field, central Flores, Indonesia. *Bulletin of the Geological Survey of Japan*, *53*(2/3), 109–138. https://doi.org/10.9795/bullgsj.53.109

Muraoka, H., Nasution, A., Urai, M., Takahashi, M., & Takashima, I. (2002b). Geochemistry of volcanic rocks in the Bajawa geothermal field, central Flores, Indonesia. *Bulletin of the Geological Survey of Japan*, *53*(2/3), 147–159. https://doi.org/10.9795/bullgsj.53.147

Nikulin, A., Bourke, J. R., Domino, J. R., & Park, J. (2019). Tracing geophysical indicators of fluid-induced serpentinization in the Pampean flat slab of Central Chile. *Geochemistry, Geophysics, Geosystems*, *20*(9), 4408–4425. https://doi.org/10.1029/2019GC008491

Nugroho, H., Harris, R., Lestariya, A. W., & Maruf, B. (2009). Plate boundary reorganization in the active Banda Arc–continent collision: Insights from new GPS measurements. *Tectonophysics*, *479*(1–2), 52–65. https://doi.org/10.1016/j.tecto.2009.01.026

Olugboji, T. M., Park, J., Karato, S. I., & Shinohara, M. (2016). Nature of the seismic lithosphere-asthenosphere boundary within normal oceanic mantle from high-resolution receiver functions. *Geochemistry, Geophysics, Geosystems*, *17*(4), 1265–1282. https://doi.org/10.1002/2015GC006214

Owens, T. J., Crotwell, H. P., Groves, C., & Oliver-Paul, P. (2004). SOD: Standing order for data. *Seismological Research Letters*, *75*(4), 515–520. https://doi.org/10.1785/gssrl.75.4.515-a

Petkovic, P., Collins, C. D. N., & Finlayson, D. M. (2000). A crustal transect between Precambrian Australia and the Timor Trough across the Vulcan Sub-basin. *Tectonophysics*, *329*(1–4), 23–38. https://doi.org/10.1016/S0040-1951(00)00186-4

Porritt, R. W., Miller, M. S., O'Driscoll, L. J., Harris, C. W., Roosmawati, N., & da Costa, L. T. (2018). Continent–arc collision in the Banda Arc imaged by ambient noise tomography. *Earth and Planetary Science Letters*, *449*, 246–258. https://doi.org/10.1016/j.epsl.2016.06.011

Pownall, J., Hall, R., & Watkinson, I. M. (2013). Extreme extension across Seram and Ambon, eastern Indonesia: Evidence for Banda slab rollback. *Solid Earth*, *4*(2), 277–314. https://doi.org/10.5194/se-4-277-2013

Rutherford, E., Burke, K., & Lytwyn, J. (2001). Tectonic history of Sumba Island, Indonesia, since the late Cretaceous and its rapid escape into the forearc in the Miocene. *Journal of Asian Earth Sciences*, *19*(4), 453–479. https://doi.org/10.1016/S1367-9120(00)00032-8

Salimbeni, S., Agostinetti, N. P., Pondrelli, S., & CIFALPS Working Group. (2021). Insights into the origin and deformation style of the continental Moho: A case-study from the Western Alps (Italy). *Journal of Geophysical Research: Solid Earth*, *126*(6), e2020JB021319. https://doi.org/10.1029/2020JB021319

Schulte-Pelkum, V., Becker, T. W., Behr, W. M., & Miller, M. S. (2021). Tectonic inheritance during plate boundary evolution in southern California constrained from seismic anisotropy. *Geochemistry, Geophysics, Geosystems*, *22*(11), e2021GC010099. https://doi.org/10.1029/2021GC010099

Schulte-Pelkum, V., Caine, J. S., Jones, J. V., III, & Becker, T. W. (2020). Imaging the tectonic grain of the northern Cordillera orogen using Transportable Array receiver functions. *Seismological Research Letters*, *91*(6), 3086–3105. https://doi.org/10.1785/0220200182

Schulte-Pelkum, V., & Mahan, K. H. (2014a). A method for mapping crustal deformation and anisotropy with receiver functions and first results from USArray. *Earth and Planetary Science Letters*, *402*, 221–233. https://doi.org/10.1016/j.epsl.2014.01.050

Schulte-Pelkum, V., & Mahan, K. H. (2014b). Imaging faults and shear zones using receiver functions. *Pure and Applied Geophysics*, *171*(11), 2967–2991. https://doi.org/10.1007/s00024-014-0853-4

Schulte-Pelkum, V., Monsalve, G., Sheehan, A., Pandey, M. R., Sapkota, S., Bilham, R., & Wu, F. (2005). Imaging the Indian subcontinent beneath the Himalaya. *Nature*, *435*(7046), 1222–1225. https://doi.org/10.1038/nature03678

Schulte-Pelkum, V., Ross, Z. E., Mueller, K., & Ben-Zion, Y. (2020). Tectonic inheritance with dipping faults and deformation fabric in the brittle and ductile southern California crust. *Journal of Geophysical Research: Solid Earth*, *125*(8), e2020JB019525. https://doi.org/10.1029/2020JB019525

Sherrington, H. F., Zandt, G., & Frederiksen, A. (2004). Crustal fabric in the Tibetan Plateau based on waveform inversions for seismic anisotropy parameters. *Journal of Geophysical Research: Solid Earth*, *109*(B2). Portico. https://doi.org/10.1029/2002jb002345

Shulgin, A., Kopp, H., Mueller, C., Lueschen, E., Planert, L., Engels, M., et al. (2009). Sunda-Banda Arc transition: Incipient continent-island arc collision (northwest Australia). *Geophysical Research Letters*, *36*(10), L10304. https://doi.org/10.1029/2009GL037533

Silver, E. A., Reed, D., McCaffrey, R., & Joyodiwiryo, Y. (1983). Back arc thrusting in the eastern Sunda arc, Indonesia: A consequence of arc-continent collision. *Journal of Geophysical Research*, *88*(B9), 7429–7448. https://doi.org/10.1029/JB088iB09p07429

Spakman, W., & Hall, R. (2010). Surface deformation and slab–mantle interaction during Banda Arc subduction rollback. *Nature Geoscience*, *3*(8), 562–566. https://doi.org/10.1038/ngeo917

Supendi, P., Nugraha, A. D., Widiyantoro, S., Abdullah, C. I., Rawlinson, N., Cummins, P. R., et al. (2020). Fate of Forearc lithosphere at arc-continent collision zones: Evidence from local earthquake tomography of the Sunda–Banda Arc transition, Indonesia. *Geophysical Research Letters*, *47*, e2019GL086472. https://doi.org/10.1029/2019GL086472

Syuhada, S., Hananto, N. D., Abdullah, C. I., Puspito, N. T., Anggono, T., & Yudistira, T. (2016). Crustal structure along Sunda-Banda Arc transition zone from teleseismic receiver functions. *Acta Geophysica*, *64*(6), 2020–2049. https://doi.org/10.1515/acgeo-2015-0098

Tate, G. W., McQuarrie, N., van Hinsbergen, D. J., Bakker, R. R., Harris, R., & Jiang, H. (2015). Australia going down under: Quantifying continental subduction during arc-continent accretion in Timor-Leste. *Geosphere*, *11*(6), 1860–1883. https://doi.org/10.1130/GES01144.1

Vergne, J. (2003). Evidence for upper crustal anisotropy in the Songpan-Ganze (northeastern Tibet) terrane. *Geophysical Research Letters*, *30*(11). https://doi.org/10.1029/2002gl016847

Zenonos, A., De Siena, L., Widiyantoro, S., & Rawlinson, N. (2019). P and S wave travel time tomography of the SE Asia-Australia collision zone. *Physics of the Earth and Planetary Interiors*, *293*, 106267. https://doi.org/10.1016/j.pepi.2019.05.010

Zenonos, A., De Siena, L., Widiyantoro, S., & Rawlinson, N. (2020). Direct inversion of S-P differential arrival times for ratio in SE Asia. *Journal of Geophysical Research: Solid Earth*, *125*(5), e2019JB019152. https://doi.org/10.1029/2019JB019152

Zhang, P., & Miller, M. S. (2021). Seismic imaging of the subducted Australian continental margin beneath Timor and the Banda Arc collision zone. *Geophysical Research Letters*, *48*(4), e2020GL089632. https://doi.org/10.1029/2020GL089632